RESEARCH ARTICLE

ADVANCED
ELECTRONIC
MATERIALS
Open Access

www.advelectronicmat.de

Direct Observation for Distinct Behaviors of Gamma-Ray Irradiation-Induced Subgap Density-of-States in Amorphous InGaZnO TFTs by Multiple-Wavelength Light Source

Jaewook Yoo, Hyeun Seung Jo, Seung-Bae Jeon, Taehwan Moon, Hongseung Lee, Seongbin Lim, Hyeonjun Song, Binhyeong Lee, Soon Joo Yoon, Soyeon Kim, Minah Park, Seohyeon Park, Jo Hak Jeong, Keun Heo, Yoon Kyeung Lee, Peide D. Ye, TaeWan Kim,* and Hagyoul Bae*

The amorphous In—Ga—Zn—O (a-IGZO) thin film transistors (TFTs) have attracted attention as a cell transistor for the next generation DRAM architecture because of its low leakage current, high mobility, and the back-end-of-line (BEOL) compatibility that enables monolithic 3D (M3D) integration. IGZO-based electronic devices used in harsh environments such as radiation exposure can be vulnerable, resulting in functional failure. Here, the behavior of subgap density-of-states (DOS) over full subgap range according to the impactful gamma-ray irradiation in a-IGZO TFTs is investigated by employing DC current–voltage ($I-V$) data with multiple-wavelength light sources. To understand the origins of the radiation effect, IGZO films have been also analyzed by x-ray photoelectron spectroscopy (XPS). Considering in-depth electrical and chemical analysis, the unexpected increase of subthreshold leakage current caused by total ionizing dose (TID) is strongly correlated with newly discovered deep-donor states ($g_{DD}^\gamma(E)$) at the specific energy level. In particular, oxygen vacancies caused by the gamma-ray irradiation give rise to undesirable electrical characteristics such as hysteresis effect and negative shift of threshold voltage (V_T). Furthermore, the TCAD simulation results based on DOS model parameters are found to exhibit good agreement with experimental data and plausible explanation including ($g_{DD}^\gamma(E)$).

1. Introduction

Memory, logic, and processor chips in the semiconductor industry are developed to meet goals oriented toward PPAC (power-performance-area-cost), with the aim of high performance, low power consumption, and reduced costs.[1] To satisfy PPAC, silicon (Si)-based complementary metal oxide semiconductors (CMOS) were scaled, however, it has caused problems of increasing leakage current and power consumption. Due to the physical limitations of Si-based CMOS, semiconductor devices have developed in several aspects, including: 1) higher dielectric constant (k) gate oxides; 2) new materials other than Si used as active layers; and 3) building transistors with 3D structures such as FinFET, GAA FETs, and multiple-stacked nanosheet FETs.[2–5] Not only these, sequential monolithic 3D (M3D) integrated circuits are designed

J. Yoo, H. Lee, S. Lim, H. Song, S. Kim, M. Park, S. Park, H. Bae
Department of Electronic Engineering
Jeonbuk National University
567 Baekje-daero, Deokjin-gu, Jeonju 54896, Republic of Korea
E-mail: hagyoul.bae@jbnu.ac.kr

H. S. Jo
Department of Electrical Engineering
Jeonbuk National University
567 Baekje-daero, Deokjin-gu, Jeonju 54896, Republic of Korea

S.-B. Jeon
Department of Electronic Engineering
Hanbat National University
125 Dongseo-daero, Yuseong-gu, Daejeon 34158, Republic of Korea

T. Moon
Department of Intelligence Semiconductor Engineering
Ajou University
Suwon 16399, Republic of Korea

B. Lee, S. J. Yoon, Y. K. Lee
Division of Advanced Materials Engineering
Jeonbuk National University
567 Baekje-daero, Deokjin-gu, Jeonju 54896, Republic of Korea

J. H. Jeong, K. Heo
Department of Semiconductor Science and Technology
Jeonbuk National University
567 Baekje-daero, Deokjin-gu, Jeonju 54896, Republic of Korea

P. D. Ye
School of Electrical and Computer Engineering
Purdue University
465 Northwestern Ave., West Lafayette, IN 47907, USA

T. Kim
School of Advanced Cross-disciplinary Studies
Department of AI Semiconductor
University of Seoul
163, Seoulsiripdae-ro, Dongdaemun-gu, Seoul 02504, Republic of Korea
E-mail: twkim@uos.ac.kr

ADVANCED
SCIENCE NEWS

www.advancedsciencenews.com

ADVANCED
ELECTRONIC
MATERIALS

www.advelectronicmat.de

to effectively improve the PPAC by reducing wiring length compared to conventional flip chips or through-silicon via (TSV) chips.[6,7] Meanwhile, back-end-of-line (BEOL) process has been introduced at a low temperature (<400 °C) to maintain the performance of the transistors in the pre-made lower layer during the M3D process.[8] Thin film transistors (TFTs) based on 2D materials and amorphous oxide semiconductors (AOSs) have been adopted as promising substances to replace the existing Si, which requires a high-temperature process. The 2D material can perform high-density integration and low-power operation of high-performance devices. The 2D materials are promising as BEOL transistor channel material for M3D DRAM application owing to the absence of dangling bonds, but unfortunately, high crystal quality films are difficult to grow on Si substrates at low temperatures.[6] Recently, there has been attention toward technology that allows for stacking AOS-based high-layer transistors with high-quality thin films that can be deposited at low temperatures using sputtering and atomic layer deposition (ALD).[9,10]

Memory devices' ability to process high capacities of information has become ever more critical due to the development of artificial intelligence (AI), including various computing programs and the Internet of Things (IoT). Dynamic random-access memory (DRAM) and static RAM (SRAM), which constitute the central processing units (CPUs) where memory devices are used intensively, require one-transistor-one-capacitor (1T1C) and six transistors (6T), respectively. AOS TFTs, i.e., amorphous-IGZO (a-IGZO), have a relatively wide bandgap (>3eV) compared to Si, which means they have a low leakage current, high mobility, and low-temperature deposition (>400 °C), making them suitable for future high-performance memory solutions that reduce single-cell size.[6,11–20] IGZO TFTs have been actively studied for display applications, but research on them as memory transistors has only recently begun. The low leakage current of a-IGZO TFTs has the advantage of being able to operate at a lower power even if the waiting time for DRAM, which is a volatile memory, to be accessed is prolonged. Z. Zhou et al. implemented ferroelectric capacitive memory cells (FCM) in which DRAM was developed into a nonvolatile memory in a 1T1C structure by vertically stacking the IGZO-based cell transistors and ferroelectric capacitors.[16] 1T1C cells have significantly improved latency and energy consumption in large FCM arrays and demonstrated the potential to be used as a high-density, low-power, non-volatile memory. S.-W. Chang et al. demonstrated for the first time an SRAM circuit constructed using six vertically stacked IGZO transistors.[17] To implement CMOS, p-type transistors were used as poly-Si materials to verify that Si and IGZO were compatible in the same process. The resulting CMOS was shown to reduce leakage power by more than four times compared to NMOS logic composed of only IGZO transistors. As previously introduced, IGZO-based memory is further being studied with the aim of applying the existing 3D memory structure, combining it with other materials, or 2T0C structure with a removed capacitor, to overcome the limitations of the existing 1T1C-based Si-memory.[18–21]

The effect of gamma-ray (γ-ray) emitted in the form of electromagnetic waves as atomic nuclei produced by radioactive decay has been investigated regarding the electrical performance and long-term reliability of semiconductor devices used in aviation, military, and aerospace applications.[22–27] Gamma-ray generates defects and electron-hole pairs (ehp) in the subgap region of the semiconductor, causing generation-recombination, carrier scattering, and charge compensation.[22] The instability induced by the irradiation of the first gamma-rays in IGZO films, they were reported to recover to performance similar to their initial state after as few as three months and as many as six months, but they should be considered seriously due to the potential for permanent and persistent exposure to the gamma-ray environment.[26] High doses of exposure to gamma-ray (aerospace shuttles, satellites, stratospheres, high-energy particle accelerators, etc.) could significantly reduce the system's life span.

Through various measurements such as $I–V$, $C–V$, and optical charge pumping, the subgap density of state (DOS) of IGZO TFTs was characterized, enabling a precise investigation of the defects in IGZO TFTs.[28–34] The optical charge pumping technique is a method of comparing the amount of charge modulation of IGZO TFTs' dark and photon states by intentionally exposing IGZO TFTs to light.[35] Compared to device characteristics in dark state, this technique can eliminate errors in the recombination of electrons that occur during device measurement, thus enabling much more accurate evaluation. Since light has higher energy as the wavelength gets shorter, multiple-wavelength light is used to analyze the distribution of oxygen vacancies (V_O) in response to the light energy within the specific subgap state.

Although previous studies have demonstrated the changes in the basic electrical properties of IGZO TFTs due to gamma-ray irradiation, the understanding of its mechanism remains incomplete.[26,27] To utilize IGZO TFTs as memory devices for current industrial applications, the long-term instability caused by high doses gamma-ray irradiation must be systematically analyzed to consider the deterioration mechanism. The previously used $C–V$ characterization techniques were not useful due to the limitations of the measurement equipment resolution in the scaled devices. In this study, we quantitatively analyze the subgap DOS change, which is the fundamental cause of the negative V_T shift and the increased leakage current in the IGZO TFTs under gamma-ray irradiation. Through the photo-responsive $I–V$ characterization with multiple-wavelength light sources, deterioration mechanisms related to pre-existed and newly-introduced oxygen vacancies were fully investigated. The validity of the measured $I–V$ data before and after gamma-ray irradiation is verified by model fitting and TCAD simulation.[36–39]

2. Result and Discussion

2.1. Structural Analysis of Gamma-Ray Irradiation in -IGZO Film

The a-IGZO film crystallized when it obtained energy that exceeded the high energy barrier. While it has been argued by C.-Y Huang et al. that the energy of gamma-ray does not affect the crystal phase because there is not enough energy beyond the kinetic barrier, there are conflicting findings published by M. B. Zalte et al. that show a-IGZO film was crystallized from gamma-ray of adequate intensity.[26,27] To analyze the effect of gamma-ray on the IGZO film directly, the IGZO-TFTs with a bottom gate electrode to which the channel is depicted can be seen in **Figure 1a**. When gamma rays were irradiated on a-IGZO film, structural analyses
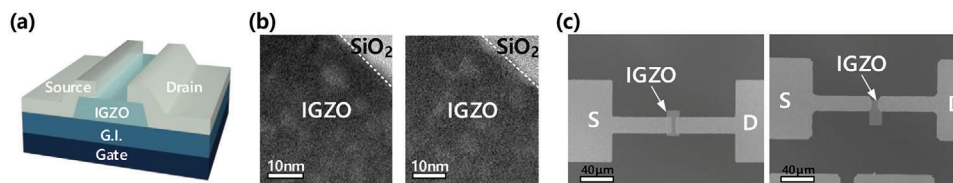
**ADVANCED
SCIENCE NEWS**

www.advancedsciencenews.com

**ADVANCED
ELECTRONIC
MATERIALS**

www.advelectronicmat.de

Figure 1. a) Schematic diagram of the bottom gate of the IGZO TFTs devices fabricated in this work. b) TEM images of the cross-sectional IGZO film Before (Left) and After (Right) gamma-ray irradiation, c) FE-SEM images of IGZO TFTs surface magnified by 400 times.

were conducted to investigate the possibility of maintaining an amorphous phase or transition to crystalline phases. Figure 1b,c shows the transmission electron microscope (TEM) and field emission-scanning electron microscope (FE-SEM) images of the cross-section and surface of the IGZO before and after gamma-ray irradiation, respectively. The IGZO film used in the analysis was also deposited under the same conditions as above, and the IGZO film components distribution was confirmed through the energy dispersive spectroscopy (EDS) mapping results shown in Figure S1 (Supporting Information). The IGZO films were investigated as to whether the amorphous state was maintained using the X-ray diffractometer (XRD) to escape the visual limit, and Figure 2a shows that crystallization was maintained as the IGZO peak had an intensity near 32° both before and after gamma-ray irradiation. Figure 2b shows the changes in surface roughness before and after the gamma-ray irradiation of the IGZO films, with a 5×5 µm² area analyzed through atomic force microscope (AFM). The root-mean-square (RMS) values of Rq and Ra exhibited a marginal increase from 0.549 to 0.563 and 0.426 to 0.437, respectively. However, this variation is considered insignificant and may be attributed to potential errors stemming from equipment conditions or the film deposition process. Based on visual analyses such as TEM and FE-SEM, along with physical properties assessments through XRD and AFM, it has been observed that gamma-ray irradiation has a negligible impact on the surface state of the IGZO films, specifically in terms of crystal structural deformation. Figure S2 (Supporting Information) is the result of analysis based on the atomic distribution depth of In, Ga, Zn, O, H, N, and Si in the IGZO film through time-of-flight secondary ion mass spectrometry (ToF-SIMS). Thus, gamma-ray caused negligible structural variation, in the surface or depth direction of the IGZO film.

2.2. Subgap DOS Model and Operation Mechanism in IGZO TFTs

The instability of AOS has been ascribed to carrier traps existing in gate insulators, interfaces, and channel layers in general. For IGZO TFTs, these traps are often considered to be primarily generated by oxygen and hydrogen deficiencies within the channel layer.[35,40,41] When the oxygen atoms of the IGZO film combined by metal–oxide (M–O) bonding diffuse to the outside, they created V_O located in the deep donor state $g_{DD}(E)$ in the middle gap area or near the valence band (VB).[42] Electrons in the VB were easily captured by V_O and produced ehp, increasing the conductivity. It was the ionized vacancies (V_O^{2+}) via a V_O ionization mechanism such as $V_O \rightarrow V_O^{2+} + 2e^-$, that resulted in one V_O emitting two free electrons, leading to a large negative V_T shift and an increased conductivity. V_O^{2+} was located in the shallow donor-like state $g_{SD}(E)$ near the CB, and helped excite the free electrons to CB. Hydrogen in the IGZO film had states of H^0, H^+, and H^- depending on the presence or absence of bound electrons. H^- was bonded to a vacant position where oxygen atoms were located during the M-O bond by external diffusion, forming a metal-hydrogen (M—H) bond. H^+ reacted with the externally diffused oxygen atom O^{2-} in a bonding formula of $H^+ + O^{2-} \rightarrow OH^- + e^-$. Hydrogen-related defects, like V_O, contributed in part to reducing the V_T, the negative movement of curves, and improving the photoconductivity by donating a single free electron located in the $g_{DD}(E)$.[35,40,41]

Figure 3a shows the schematic of the weakly bonded M-O and electron transport when operating as a subgap DOS of the IGZO TFTs. The $g_{CB}(E)$ in the subgap of the IGZO TFTs, an n-type semiconductor, consisted of a tail acceptor state $g_{TA}(E)$, $g_{SD}(E)$, and a deep acceptor state $g_{DA}(E)$; with $g_{VB}(E)$ being distributed as the tail
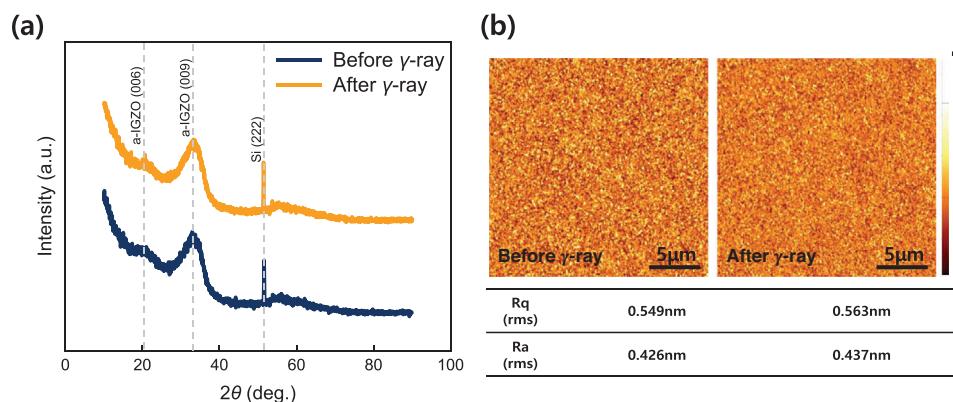

Figure 2. a) XRD spectra of the IGZO film Before/After gamma-ray irradiation. b) AFM topological images and RMS values.
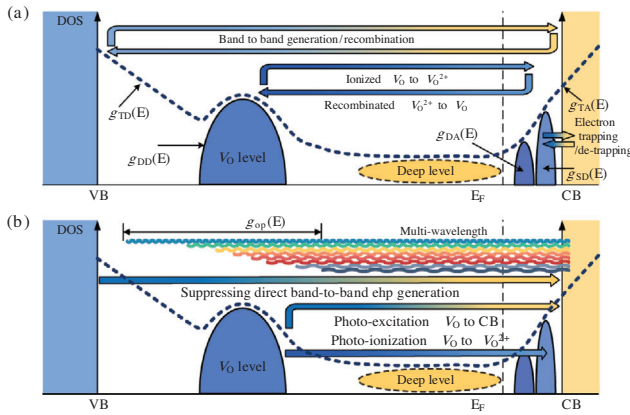
	Before γ-ray	After γ-ray
Rq (rms)	0.549nm	0.563nm
Ra (rms)	0.426nm	0.437nm

**ADVANCED
SCIENCE NEWS**

www.advancedsciencenews.com

**ADVANCED
ELECTRONIC
MATERIALS**

www.advelectronicmat.de

Figure 3. a) Schematic diagram illustrating the ionization of V_O and behavior of electrons across the full energy spectrum. b) Schematic representation of the ionization of V_O and electron excitation processes induced by interactions with an incident multi-wavelength light source.

donor state $g_{TD}(E)$ and $g_{DD}(E)$. In AOS, V_O was located in $g_{DD}(E)$ and V_O^{2+} was known to be $g_{SD}(E)$ and $g_{DA}(E)$. Therefore, the subgap DOS in Figure 3a was modeled using the following equation:

$$g_{CB}(E) = g_{TA}(E) + g_{SD}(E) + g_{DA}(E)$$

$$= N_{TA} \exp\left(-\frac{E_C - E}{kT_{TA}}\right) + N_{SD} \exp\left(-\left(\frac{E_C - E_{SD} - E}{kT_{SD}}\right)^2\right)$$

$$+ N_{DA} \exp\left(-\left(\frac{E_C - E_{DA} - E}{kT_{DA}}\right)^2\right) (\text{cm}^{-3}\text{eV}^{-1}) \quad (1)$$

$$g_{VB}(E) = g_{TD}(E) + g_{DD}(E)$$
$$= N_{TD} \exp\left(-\frac{E - E_V}{kT_{TD}}\right) + N_{DD} \exp\left(-\left(\frac{E - E_{DD} - E_O}{kT_{DD}}\right)^2\right) (\text{cm}^{-3}\text{eV}^{-1}) \quad (2)$$

The parameters used in the equation were later used to fit the subgap DOS that was changed from the gamma-ray irradiation. Figure 3b presents a schematic diagram illustrating the potential electron behaviors within the subgap DOS of IGZO when illuminated by a light source. Figure 3b is predominantly utilized to observe the subgap DOS across the full-range energy band diagram. If light has enough energy to reach the V_O level, the electrons of V_O are excited to CB or ionized to $g_{SD}(E)$, contributing to an improve in the conductivity.

2.3. Electrical Characteristic of Gamma-Ray Irradiation in IGZO TFTs

To evaluate the effect of the gamma-ray irradiation on the IGZO TFTs, we measured the transfer (I_{dark}), I_G, and output characteristics of the IGZO TFTs stabilized in the dark state, which corresponded to **Figure 4a,b**. From Figure 4a, showing the results after gamma-ray irradiation, a $g_{SD}(E)$ had been created on the IGZO film, demonstrated by the appearance of a hump.[43,44] Figure 4c,d,e showed the changes in V_T, field effect mobility (μ_{FE}), and SS of the ten IGZO TFTs from gamma-ray irradiation, respectively. V_T tended to shift negatively, and μ_{FE} had not changed

significantly in most devices due to transconductance. SS appeared to be improved by the gamma-ray, such as the transfer characteristics shown in Figure 4a. The IGZO TFTs' hysteresis is related to the difference in the charging and discharging cycles of the structural defects under the gate voltage (V_G). The increase in the V_T shift from before and after the gamma-ray hysteresis contrasted with the change in SS.

The energy bandgap (E_{BDG}) was calculated using a Tauc-plot based on a spectroscopic ellipsometer (SE).[45] The obvious difference before and after gamma-ray irradiation on the ultraviolet photoelectron spectroscopy (UPS) spectrum, can be observed in Figure 4g,h. From the UPS spectrum, the offset (E_{FV}) between the Fermi Energy Level (E_F) and the valence band maximum (VBM) energy level rises from 2.67 to 2.79 eV, indicating a significant change in the bandgap energy (E_{BDG}).[45] In Figure 4i, the E_{BDG} of the IGZO film before and after gamma-ray irradiation, through the same deposition process, was 3.22 and 3.20 eV, showing no significant change.[46] The relationship between the E_{BDG} and E_{FV} was deduced by the band offset (E_{CF}) between the conduction band minimum (CBM) energy level and E_F. The calculated E_F showed that after gamma-ray irradiation, the E_F reduced energy level difference between the CB, indicating that electrons can be excited to the CB with only low energy, increasing the electron concentration.

2.4. Observation of DOS Formation in IGZO TFTs from Gamma-Ray Irradiation

As mentioned above, the V_O caused various instabilities and was estimated to be the subgap DOS of IGZO TFTs through $I-V$, $C-V$ characterization, and optical charge pumping technology. A recent on-chip spectroscopy technique for obtaining the subgap DOS was introduced using ultrabroadband photoconduction (UBPC) microscopy. The UBPC used a self-made electrical probe to detect noise at each illumination wavelength using the current pre-amplifier and lock-in amplifier and monitored the subgap DOS by finding the photoconductivity (PC).[47] Based on a high accuracy assumption compared to existing methods, it was possible to cover all energy ranges, but it was difficult to use universally because they required special installations. To compensate, the characterization of the IGZO subgap DOS was proposed in this study by combining the previously known $I-V$ based DOS extraction methods and multiple-wavelengths to propose a unified observation method. The irradiated multiple-wavelengths had energy in the subgap and the optical power of each wavelength was confirmed in Table S1 (Supporting Information). The irradiated multiple-wavelengths from 900 to 460 nm corresponded to 1.4 to 2.7 eV. The shorter the wavelength, the closer the photon-affected states are to the valence band stated $g_{VB}(E)$. The V_O located close to $g_{VB}(E)$ was inferred as a response to the multiple-wavelength of the optical illumination states $g_{op}(E)$. Since the formation energy of V_O in the IGZO films was estimated to be ≈4 eV, according to thermodynamic calculations, V_O was significantly less likely to be formed from light irradiation.[43,48] **Figure 5a,b** shows the transfer (I_{opt}) characteristics of responding to a single IGZO TFTs before and after gamma-ray irradiation for various light wavelengths. The shorter the irradiated wavelength, the more ehp generation was promoted. As a result, the electrons were excited
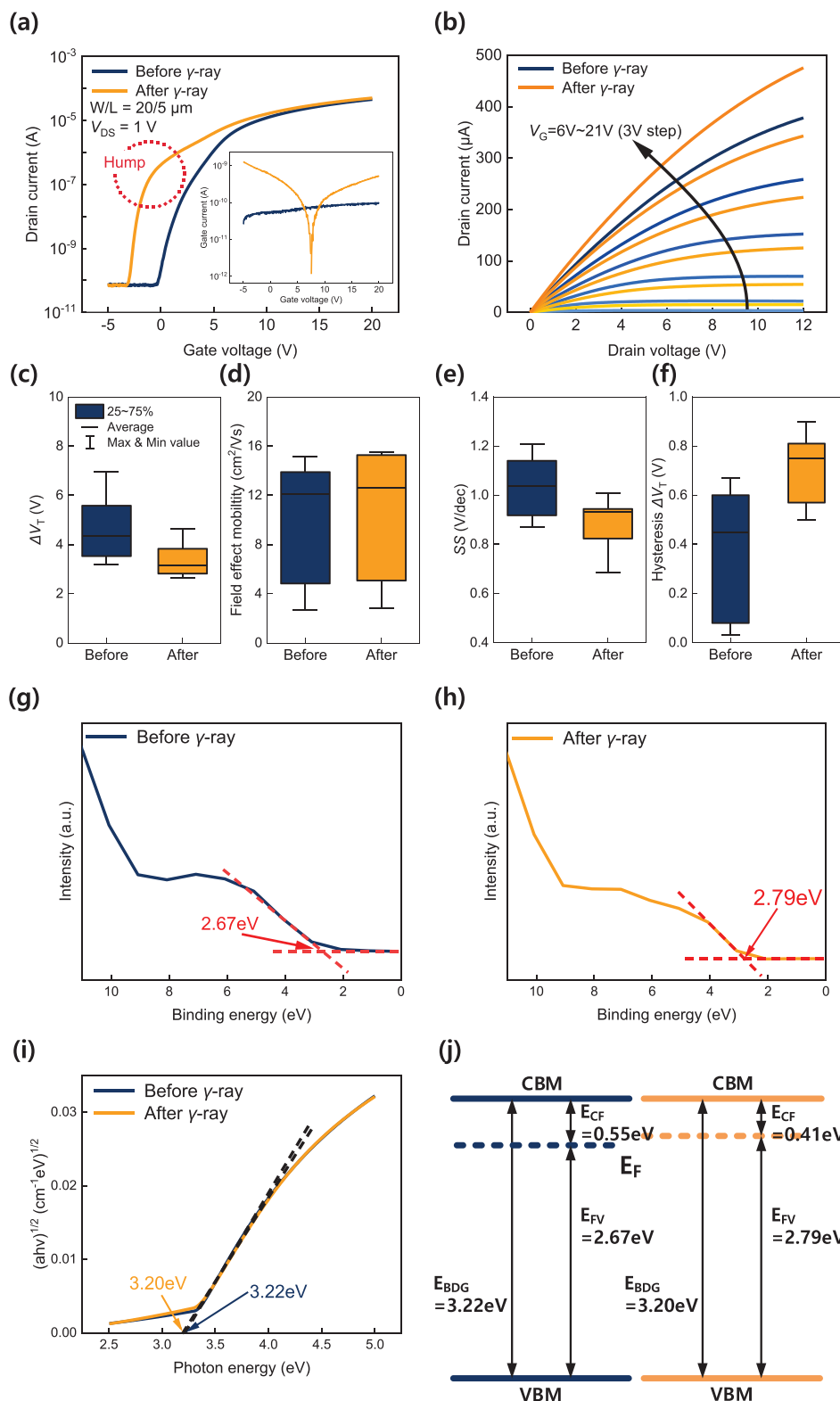
**ADVANCED
SCIENCE NEWS**

www.advancedsciencenews.com

**ADVANCED
ELECTRONIC
MATERIALS**
Open Access

www.advelectronicmat.de

Figure 4. Electrical characteristics of the IGZO TFTs before and after gamma-ray irradiation (indigo/yellow): a) the transfer and gate leakage characteristics (inset), b) the output characteristics, c) shifted V_T, d) μ_{FE}, e) SS, and f) the shifted V_T in the hysteresis data. Extracted valence band edge analysis by UPS results g) before and h) after the gamma-ray irradiation. i) Tauc plot results by the SE spectra of the IGZO film before and after gamma-ray irradiation. j) Corresponding band alignment of the IGZO film before and after gamma-ray irradiation.
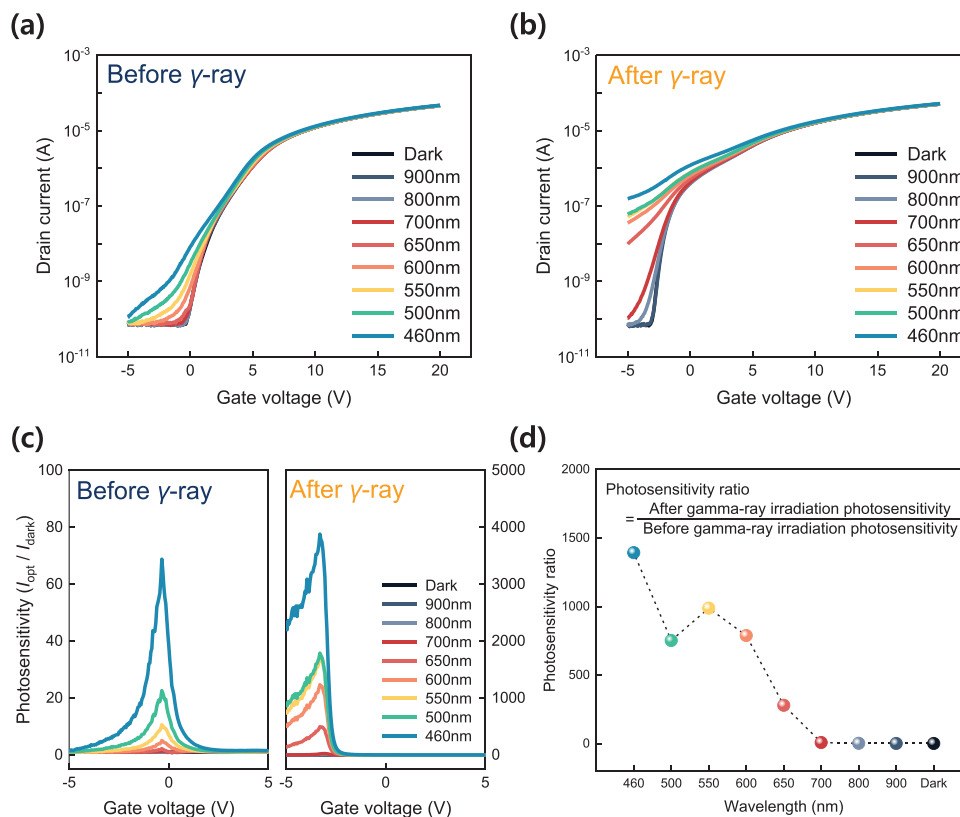
Figure 5. Transfer characteristics of the IGZO TFT in the dark and after being illuminated with multiple-wavelengths, a) before and b) after gamma-ray irradiation. c) Photosensitivity versus V_G under gamma-ray irradiation. d) Plot photosensitivity ratio under gamma-ray irradiation.

to the CB, increased photoconductivity, and the holes were accumulated at the interface under negative voltage, causing V_T to shift negatively. Figure 5c is the photosensitivity (I_{opt}/I_{dark}) graph before and after gamma-ray irradiation of the IGZO TFTs. Photosensitivity refers to the result of photons, previously captured electrons, and electrons generated when V_O was ionized were excited as CB in the subgap DOS. Figure 5d is the result of plotting the peak in Figure 5c. Before and after gamma-ray irradiation, the area of photosensitivity that varies as V_G changes is shown in Figure S3 (Supporting Information). The peak was modeled for each wavelength, and the photosensitivity ratio increases as the wavelength decreases. In the dark state, no large reaction occurs up to a wavelength of 700 nm. Previously known photocurrent of IGZO TFT is studied to increase rapidly at the 550 to 650nm wavelength.[37,43,45,53] Although the ratio decreases partially at 500 nm wavelength, it still means an increase in V_O induced by gamma-ray irradiation and is similar to the distribution of V_O along the Gaussian function. This trend was caused by photons reacting to the subgap DOS, and by estimating the electrons excited to CB, where the subgap DOS distribution of the IGZO TFTs modulated by gamma-ray irradiation can be seen.[49]

The distribution of the subgap DOS modulated by gamma-ray was characterized through I–V based extraction techniques. The I–V based extraction techniques can be controversial in specifying flat-band voltage (V_{FB}) to extract the subgap DOS. Therefore, the V_{FB} was extracted based on the Shockley-read-Hall (SRH) I_{G-R} theory.[30,50] V_{FB} and V_T were extracted as -

0.3/6.5V before gamma-ray irradiation and -3.2/5.5V after irradiation. When the IGZO TFTs were irradiated with gamma-ray, both V_T and V_{FB} shifted negatively. The V_{FB} was extracted via generation-recombination current (I_{G-R}) results, measurement methods, and mechanisms were introduced in detail in Figure S4 (Supporting Information). The $g_A(E)$ of the IGZO TFTs extracted in the dark condition was plotted as the scatter (Black) in **Figure 6a,b**. In the dark condition, the m-factor representing the effect of controlling the surface potential by the gate voltage was used. The coupling model consisted of a substrate capacitance (C_{Free}) that existed in the form of a free electron of CB and a localized capacitance (C_{LOC}) that included an interface and a bulk trap. After gamma-ray irradiation, extracted with such a model, $g_A(E)$ increased compared to before the gamma-ray irradiation, meaning that the gamma-ray irradiation affected the conductivity of the IGZO TFTs. When the light was illuminated onto the IGZO TFTs, in addition to the pre-existing electrons, it composed a parasitic capacitance ($C_{LOC,ph}$) that reacted to the illumination. The shorter the wavelength to be illuminated the more the reactive defects increased, and the m-factor in the subthreshold region derived from the generated free electrons also increased proportionally. The $g_{op}(E)$ reacted according to the illuminated wavelength corresponding to the sum of the energy of the multiple-wavelength and the energy of the surface potential, as shown in Figure 6a,b. Intuitive observations were expressed as scatters with the unique color of the wavelength. The $g_{op}(E)$ was modeled using the same voltage range as the dark electricity
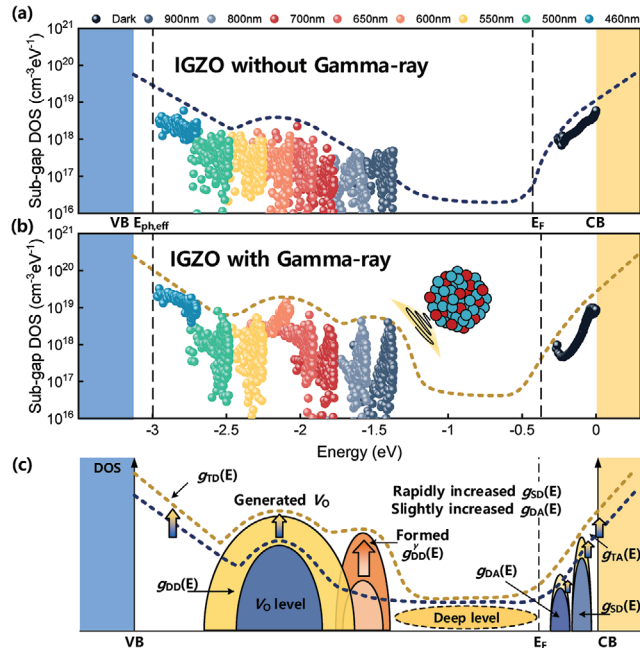
2300906 (6 of 10)

**ADVANCED
SCIENCE NEWS**

www.advancedsciencenews.com

**ADVANCED
ELECTRONIC
MATERIALS**
Open Access

www.advelectronicmat.de

Figure 6. Distribution of subgap DOS in IGZO TFTs as observed with multiple-wavelength light a) before and b) after gamma-ray irradiation. c) Schematic illustration of the increased V_o, $g_{SD}(E)$, and $g_{DA}(E)$ originating from gamma-ray irradiation in IGZO TFTs.

condition, and the m-factor that reacted from a shorter wavelength was eliminated with the m-factor that reacted from a longer wavelength, deviating from the effects of the previously generated free electrons and localized subgap DOS. The subgap DOS before and after gamma-ray irradiation characterized by $I-V$ was estimated as a dotted line, which was similar to the IGZO films subgap DOS demonstrated in other studies.[51] Comparing the modeled subgap DOS before and after gamma-ray irradiation in Figure 6c, it was estimated that the V_O concentration in the IGZO TFTs significantly increased by gamma-ray irradiation. In addition, when the gamma-ray was irradiated to the IGZO TFTs, a deep-donor state induced from gamma-ray $g_{DD}^{\gamma}(E)$ that had not been seen before was additionally formed. The conductivity and switching properties of the IGZO TFTs appeared to be improved by the gamma-ray, as shown in Figure 4a,e, as the ionization of the increased V_O boosted the $g_{SD}(E)$ and $g_{DA}(E)$, and promoted the production of ehp before illumination. As the estimated subgap DOS shows in Figure 4f, the gamma-ray increased the instability of the IGZO TFTs, which was considered a cause of serious deterioration.

As shown in **Figure 7a,b**, to identify the oxygen-related defects in a 50 nm thick IGZO film modulated by gamma-ray, the O 1s peak of the IGZO film was intensively examined through the X-ray photoelectron spectrometer (XPS) depth profile after gamma-ray irradiation. The O 1s spectra of the IGZO films for each sample were extracted by deconvolution to Gaussian peaks for M-O, V_O, and O—H, with centers at 530.2, 531.2, and 532.3 eV. For C 1s with 284.8 eV, the reference peak was used to correct the binding energy peak position of the peak, so that the O 1s peak was not overestimated. The area ratios of the individual peaks were

compared before and after gamma-ray irradiation, with the M-O bonds decreasing from 51.8 to 31.2% and the V_O increasing from 34.5 to 52.4%. This demonstrated that gamma-ray was responsible for breaking the M-O bonds, generating V_O, and that the electrons were actively excited into the CB within the IGZO film from the further ionized V_O. These electrons increased the O-H bond slightly from 13.7 to 16.4%, and, because the generated O—H bond was located in a state close to the VBM, the increase and distribution of the VBM state expanded and the $g_{DD}(E)$ associated with the hydrogen bonding increased, contributing to the increase in the conductivity of the film. The components of the IGZO film with oxygen can be seen in Figure S5 (Supporting Information). A slight shift to low binding energy was observed in the spectra of all constituents, which is known to be related to the crystallographic structure and oxygen binding of metal atoms In Figure 7 and Figure S5 (Supporting Information), the shift occurred at all peaks to a low binding energy of 0.3 to 0.4 eV, indicating the reduction of metal ions. However, the rise in E_F derived from the UPS analysis implies the result of binding energy shifting to high. As a result, gamma-ray irradiation on IGZO films means that V_O formation and ionization proceed simultaneously and is consistent with the results observed in Figure 6.

The $g_{CB}(E)$ before and after gamma-ray irradiation was quantitatively modeled by Equation (1) as shown in **Figure 8a**. All states constituted $g_{CB}(E)$ increased compared to before irradiation, which was especially increased for $g_{SD}(E)$, which was known to contribute to conductivity. The subgap DOS extracted through the multiple-wavelength was quantitatively investigated through TCAD simulation and confirmed in Figure 8b. The $g_{CB}(E)$ extracted from the model were used as the parameters of the simulation, and the interface trap density was fixed at 5×10^{12} cm^{-2}eV^{-1}. The Gaussian function used to fit the $g_{DD}(E)$ was used, and the simulation results showed that the peak and variance of the Gaussian distribution increased. Furthermore, the $g_{DD}^{\gamma}(E)$ induced from gamma-ray irradiation in Figure 6b was further modeled as a Gaussian function and reflected in TCAD simulation, and the parameters used for the model and TCAD fitting were summarized in Table S2 (Supporting Information).[52] Compared to the previously distributed V_O, the V_O generated from the gamma-ray was ionized by less energy, increasing the trapping/de-trapping of electrons. The results of the TCAD simulation were consistent with the results of the subgap DOS extracted through the previously extracted multiple-wavelength, which implied that the corresponding extraction method was valid.

3. Conclusion

We investigated IGZO TFTs using in-depth chemical and electrical analysis of the deterioration mechanism induced by gamma-ray irradiation. The gamma-ray-induced subgap DOS in IGZO TFTs was analyzed using the individual $I-V$ characteristics responding to multiple-wavelength light sources. The gamma-ray significantly affect the increased of subgap DOS associated with V_o in IGZO TFTs in the full subgap range from CBM to VBM including the additionally discovered $g_{DD}^{\gamma}(E)$ that has never been reported. The gamma-ray-induced V_o was readily ionized by photons with less energy than before the irradiation and actively involved in the trapping/de-trapping

**ADVANCED
SCIENCE NEWS**

www.advancedsciencenews.com

**ADVANCED
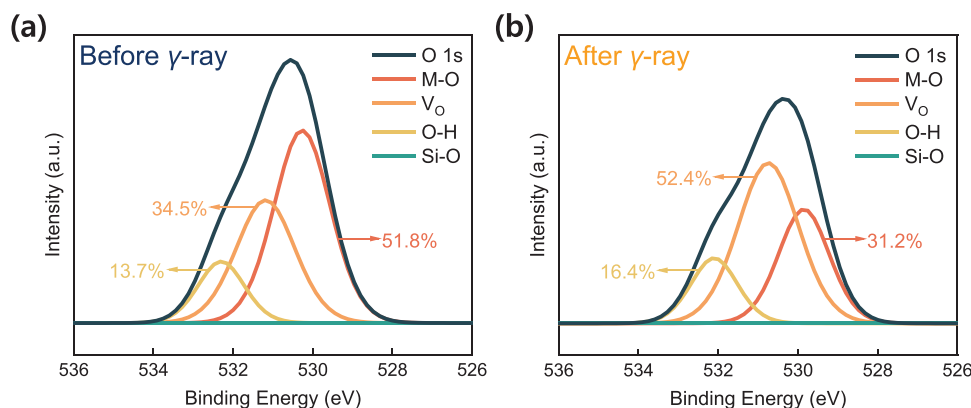ELECTRONIC
MATERIALS**

www.advelectronicmat.de

Figure 7. XPS results show the O 1s spectra in the IGZO film a) before and b) after gamma-ray irradiation.

mechanism of electrons. The subgap DOS derived from $I–V$ characteristics using multi-wavelength light sources has been examined for validity through TCAD simulation. Based on these results, the instability derived from gamma-ray should be carefully considered to be more severe, such as fatal gamma-ray dose, accelerated device scaling, and future 2T0C DRAM architecture.

4. Experimental Section

Device Fabrication: An n-type silicon substrate doped with 10^{17} or more boron was used, and the SiO_2 grown to 50 nm through thermal growth served as a gate insulator. After cleaning the substrate with acetone-isopropyl alcohol (IPA)-methanol for 5 min each, the IGZO film was deposited to a thickness of 50 nm through a radio frequency (RF) sputter at room temperature. In, Ga, and Zn were sputtered at a 1:1:1 ratio, and the gas flow of Ar/O_2 was 19/3 sccm at a substrate temperature 100 °C and a working pressure of 7×10^{-3} Torr. Through UV exposure, the IGZO channel, source, and drain electrode were patterned sequentially, and a thickness of indium tin oxide (ITO) 150 nm was deposited to a size of $150 \times 150\ \mu m^2$ using an e-beam evaporator. After ITO deposition, a lift-off process was performed using acetone, and the IGZO film was annealed for 1 hour in air ambient (400 °C) using a furnace.

Gamma-Ray Irradiation: Gamma-ray were emitted from the Co^{60} chamber (KAERI, Korea), with a dose rate of 300 Gy/hr, resulting in a total dose of 500 Gy. All devices and IGZO films used were simultaneously irradiated at room temperature with the same intensity, and no bias was applied.

Film Analysis: A TEM (Tecnai F30 S-Twin; FEI) and FE-SEM (S-4800; Hitachi) were used to visually identify the defects that occurred when the gamma-ray irradiated the IGZO TFTs. An AFM (XE-100; Park Systems), ToF-SIMS (IMS 7f; CAMECA), and XRD (SmartLab; Rigaku, Corp.) analyzed the structural changes in the physical properties, such as the surface roughness, binding ions, and the crystal structure of the IGZO thin films irradiated from the gamma-ray. An XPS (K-Alpha+; ThermoFisher Scientific) and SE (M2000D; Woollam) were used to evaluate the chemical bonding transition and characterize the bandgap and Fermi levels of the IGZO films.

Device Measurement, Characterization: To accurately examine the impact of gamma-ray on the IGZO TFTs, initial measurements were taken right after the fabrication process. Afterward, gamma-ray irradiation and post-irradiation measurements were carried out continuously. Ten devices of the same scale were measured with Keithley 4200A equipment in a room-temperature vacuum chamber. To avoid the influence of natural light, the chamber was kept in a dark state for 3 min before the measurement was performed. The light wavelength was varied using light from a TLS130B-300X (Light Source, Newport) lamp to reduce the wavelength, using a spectrometer, in 50 nm increments from near-infrared (900 nm) to
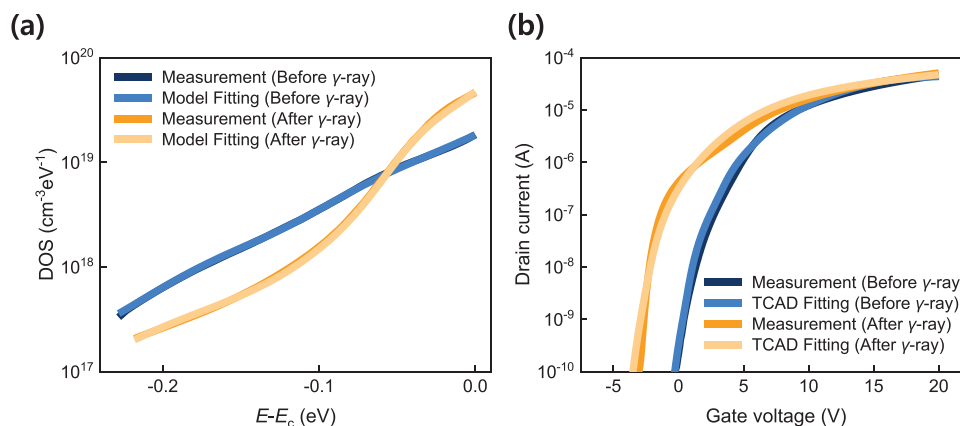

Figure 8. Fitting analysis results showing the subgap DOS distribution of the IGZO film before and after gamma-ray irradiation. a) Comparison of the subgap DOS for $I–V$ extraction method and the model fitting. b) Comparison between the measured and simulated data incorporating the extracted subgap DOS.

**ADVANCED
SCIENCE NEWS**

www.advancedsciencenews.com

**ADVANCED
ELECTRONIC
MATERIALS**
Open Access

www.advelectronicmat.de

blue-light (460 nm). Irradiation from short-wavelength illumination could lead to persistent photoconductivity (PPC) problems caused by unwanted electrical conductivity as the electron-hole pairs formed from the light were not spontaneously recombined.[53] To prevent PPC, a lamp with a power of 300 W was floated above the device at a height of 1 mm, and each time the wavelength length was changed the thin film was given enough time to react to the light. The SS, μ_{FE}, and hysteresis were examined in compliance with the theory of gradual channel approximation. The V_{FB} and the V_T defined to extract the DOS were characterized using the same criteria through the I_{G-R} and constant current method, respectively.

Simulation: The $I-V$ characterization and subgap DOS observed with a multiple-wavelength light source were validated by equation model fitting and simulation by Silvaco-ATLAS TCAD.

Supporting Information

Supporting Information is available from the Wiley Online Library or from the author.

Conflict of Interest

The authors declare no conflict of interest.

Data Availability Statement

Research data are not shared.

[1] M. Moore, International Roadmap for Devices and Systems (IRDS), https://irds.ieee.org/images/files/pdf/2021/2021IRDS_MM.pdf (accessed: November 2021).

[2] S. Yang, K. Liu, Y. Xu, L. Liu, H. Li, T. Zhai, *Adv. Mater.* **2023**, *35*, 2207901.

[3] S. E. Kim, J. Y. Sung, J. D. Jeon, S. Y. Jang, H. M. Lee, S. M. Moon, J. G. Kang, H. J. Lim, H.-S. Jung, S. W. Lee, *Adv. Mater. Technol.* **2022**, *8*, 2200878.

[4] G. Bae, D.-I. Bae, M. Kang, S. M. Hwang, S. S. Kim, B. Seo, T. Y. Kwon, T. J. Lee, C. Moon, Y. M. Choi, K. Oikawa, S. Masuoka, K. Y. Chun, S. H. Park, H. J. Shin, J. C. Kim, K. K. Bhuwalka, D. H. Kim, W. J. Kim, J. Yoo, H. Y. Jeon, M. S. Yang, S.-J. Chung, D. Kim, B. H. Ham, K. J. Park, W. D. Kim, S. H. Park, G. Song, Y. H. Kim, et al., *2018 IEEE International Electron Devices Meeting (IEDM 2018)*, San Francisco, CA, USA December **2018**.

[5] J. Hur, B.-H. Lee, M.-H. Kang, D.-C. Ahn, T. Bang, S.-B. Jeon, Y.-K. Choi, *IEEE Electron Device Lett.* **2016**, *37*, 541.

[6] T. Kim, C. H. Choi, J. S. Hur, D. Ha, B. J. Kuh, Y. Kim, M. H. Cho, S. Kim, J. K. Jeong, *Adv. Mater.* **2023**, *35*, 2204663.

[7] P.-Y. Liao, D. Zheng, S. Alajlouni, Z. Zhang, M. Si, J. Zhang, J.-Y. Lin, T. I. Feygelson, M. J. Tadjer, A. Shakouri, P. D. Ye, *IEEE Trans. Electron Devices.* **2023**, *70*, 2052.

[8] J. W. Park, B. H. Kang, H. J. Kim, *Adv. Funct. Mater.* **2020**, *30*, 1904632.

[9] M. H. Cho, C. H. Choi, J. K. Jeong, *J. Soc. Inf. Disp.* **2022**, *30*, 175.

[10] P.-Y. Liao, S. Alajlouni, M. Si, Z. Zhang, Z. Lin, J. Noh, C. Wilk, A. Shakouri, P. D. Ye, presented at *IEEE Symp. on VLSI Technology and Circuits (VLSI Technology and Circuits 2022)*, Honolulu, HI, USA June **2022**.

[11] W. Lu, Z. Zhu, K. Chen, M. Liu, B.-M. Kang, X. Duan, J. Niu, F. Liao, W. Dan, X.-S. Wu, J. Son, D.-Y. Xiao, G.-L. Wang, A. Yoo, K.-Y. Cao, D. Geng, N. Lu, G. Yang, C. Zhao, L. Li, M. Liu, in 2022 International Electron Devices Meeting (IEDM), IEEE, San Francisco, CA, USA **2022**.

[12] H. Hosono, *Nat. Electron.* **2018**, *1*, 428.

[13] H. Yoo, I. S. Lee, S. Jung, S. M. Rho, B. H. Kang, H. J. Kim, *Adv. Mater.* **2021**, *33*, 2006091.

[14] H. Bae, T. Moon, S. G. Nam, K.-H. Lee, S. Kim, S. Hong, D.-H. Choe, S. Jo, Y. Lee, J. Heo, presented at *2021 Symposium on VLSI Technology*, Kyoto, Japan, June **2021**.

[15] K. Nomura, H. Ohta, A. Takagi, T. Kamiya, M. Hirano, H. Hosono, *Nature.* **2004**, *432*, 488.

[16] Z. Zhou, L. Jiao, Q. Kong, Z. Zheng, K. Han, Y. Chen, C. Sun, B.-Y. Nguyen, X. Gong, presented at *2023 IEEE Symposium on VLSI Technology and Circuits (VLSI Technology and Circuits)*, Kyoto, Japan, June **2023**.

[17] S.-W. Chang, T.-H. Lu, C.-Y. Yang, C.-J. Yeh, M.-K. Huang, C.-F. Meng, P.-J. Chen, T.-H. Chang, Y.-S. Chang, J.-W. Jhu, T.-C. Hong, C.-C. Ke, X.-R. Yu, W.-H. Lu, M. A. Baig, T.-C. Cho, P.-J. Sung, C.-J. Su, F.-K. Hsueh, B.-Y. Chen, H.-H. Hu, C.-T. Wu, K.-L. Lin, W. C.-Y. Ma, D. D. Lu, K.-H. Kao, Y.-J. Lee, C.-L. Lin, K.-P. Huang, K.-M. Chen, et al., *IEEE Trans. Electron Devices* **2022**, *69*, 2101.

[18] J. Zhang, Z. Zhang, Z. Lin, K. Xu, H. Dou, B. Yang, X. Zhang, H. Wang, P. D. Ye, *2023 IEEE Symposium on VLSI Technology and Circuits (VLSI Technology and Circuits)*, Kyoto, Japan, June **2023**.

[19] J. Guo, K. Han, S. Subhechha, X. Duan, Q. Chen, D. Geng, S. Huang, L. Xu, J. An, G. S. Kar, X. Gong, L. Wang, L. Li, M. Liu, presented at *2021 IEEE International Electron Devices Meeting (IEDM 2021)*, San Francisco, CA, USA December **2021**.

[20] A. Belmonte, H. Oh, N. Rassoul, G. L. Donadio, J. Mitard, H. Dekkers, R. Delhougne, S. Subhechha, A. Chasin, M. J. van Setten, L. Kljucar, M. Mao, H. Puliyalil, M. Pak, L. Teugels, D. Tsvetanova, K. Banerjee, L. Souriau, Z. Tokei, L. Goux, G. S. Kar, *2020 IEEE International Electron Devices Meeting (IEDM)*, San Francisco, CA, USA, December **2020**.

[21] J. Yoo, H. Song, H. Lee, S. Lim, S. Kim, K. Heo, H. Bae, *Electronics.* **2023**, *12*, 2297.

[22] J. R. Schwank, M. R. Shaneyfelt, D. M. Fleetwood, J. A. Felix, P. E. Dodd, P. Paillet, V. Ferlet-Cavrois, *IEEE Trans. Nucl. Sci.* **2008**, *55*, 1833.

[23] J.-P. Colinge, *FinFETs and Other Multi-Gate Transistors*, Vol. *73*, Springer, New York **2008**.

[24] M. H. Wong, A. Takeyama, T. Makino, T. Ohshima, K. Sasaki, A. Kuramata, S. Yamakoshi, M. Higashiwaki, *Appl. Phy. Lett.* **2018**, *112*, 023503.

[25] H. Bae, S. G. Nam, T. Moon, Y. Lee, S. Jo, D.-H. Choe, S. Kim, K.-H. Lee, J. Heo, present at IEDM, San Francisco, CA, USA **2020**.

[26] M. B. Zalte, V. Kumar, S. G. Surya, M. S. Baghini, *IEEE Sens. J.* **2021**, *21*, 10667.

[27] C.-Y. Huang, *J. Non-Cryst. Solids.* **2020**, *546*, 120292.

[28] J. Yao, N. Xu, S. Deng, J. Chen, J. She, H.-P. D. Shieh, P.-T. Liu, Y.-P. Huang, *IEEE Trans. Electron Devices.* **2011**, *58*, 1121.

[29] S. Jun, C. Jo, H. Bae, H. Choi, D. H. Kim, D. M. Kim, *IEEE Electron Device Lett.* **2013**, *34*, 641.

[30] H. Bae, J. Noh, S. Alghamdi, M. Si, P. D. Ye, *IEEE Electron Device Lett.* **2018**, *39*, 1708.

[31] H. Bae, H. Choi, S. Jun, C. Jo, Y. H. Kim, J. S. Hwang, J. Ahn, S. Oh, J.-U. Bae, S.-J. Choi, D. H. Kim, D. M. Kim, *IEEE Electron Device Lett.* **2013**, *34*, 1524.

[32] G. W. Yang, J. Park, S. Choi, C. Kim, D. M. Kim, S.-J. Choi, J.-H. Bae, I. H. Cho, D. H. Kim, *IEEE Trans. Electron Devices.* **2022**, *69*, 166.

[33] H. Bae, H. Seo, S. Jun, H. Choi, J. Ahn, J. Hwang, J. Lee, S. Oh, J.-U. Bae, S.-J. Choi, D. H. Kim, D. M. Kim, *IEEE Trans. Electron Devices.* **2014**, *61*, 3566.

[34] J. T. Jang, J. Park, B. D. Ahn, D. M. Kim, S. J. Choi, H. S. Kim, D. H. Kim, *ACS Appl. Mater. Interfaces.* **2015**, *7*, 15570.

[35] K. Ide, K. Nomura, H. Hosono, T. Kamiya, *Phys. Status Solidi A.* **2019**, *216*, 1800372.

[36] M. M. Billah, M. D. H. Chowdhury, M. Mativenga, J. G. Um, R. K. Mruthyunjaya, G. N. Heiler, T. J. Tredwell, J. Jang, *IEEE Electron Device Lett.* **2016**, *37*, 1442.

[37] H. Lee, J. Kim, J. Kim, S. K. Kim, Y. Lee, J.-Y. Kim, J. T. Jang, J. Park, S.-J. Choi, D. H. Kim, D. M. Kim, *IEEE Electron Device Lett.* **2017**, *38*, 584.

[38] M. M. Billah, M. M. Hasan, M. Chun, J. Jang, *IEEE Electron Device Lett.* **2016**, *37*, 1442.

[39] X. Duan, K. Huang, J. Feng, J. Niu, H. Qin, S. Yin, G. Jiao, D. Leonelli, X. Zhao, Z. Wang, W. Jing, Z. Wang, Y. Wu, J. Xu, Q. Chen, X. Chuai, C. Lu, W. Wang, G. Yang, D. Geng, L. Li, M. Liu, *IEEE Trans. Electron Devices.* **2022**, *69*, 2196.

[40] J. K. Jeon, J. G. Um, S. Lee, J. Jang, *AIP Adv.* **2017**, *7*, 125110.

[41] D.-G. Kim, J.-U. Kim, J.-S. Lee, K.-S. Park, Y.-G. Chang, M.-H. Kim, D.-K. Choi, *RSC Adv.* **2019**, *9*, 20865.

[42] A. de J de Meux, A. Bhoolokam, G. Pourtois, J. Genoe, P. Heremans, *Phys. Status Solidi A.* **2017**, *214*, 1600889.

[43] M. Mativenga, F. Haque, M. M. Billah, J. G. Um, *Sci. Rep.* **2021**, *11*, 14618.

[44] D.-G. Kim, W.-B. Lee, S. Lee, J. Koh, B. Kuh, J. S. Park, *ACS Appl. Mater. Interfaces.* **2023**, *15*, 36550.

[45] B. H. Kang, W.-G. Kim, J. Chung, J. H. Lee, H. J. Kim, *ACS Appl. Mater. Interfaces.* **2018**, *10*, 7223.

[46] X. F. Chen, G. He, M. Liu, J. W. Zhang, B. Deng, P. H. Wang, M. Zhang, J. G. Lv, Z. Q. Sun, *J. Alloy. Compd.* **2014**, *615*, 636.

[47] G. W. Mattson, K. T. Vogt, J. F. Wager, M. W. Graham, *Adv. Funct. Mater.* **2023**, *33*, 2300742.

[48] J. Shi, J. Zhang, L. Yang, M. Qu, D.-C. Qi, K. H. L. Zhang, *Adv. Mater.* **2021**, *33*, 2006230.

[49] A. Abliz, D. Wan, J.-Y. Chan, L. Xu, J. He, Y. Yang, H. Duan, C. Liu, C. Jiang, H. Chen, T. Guo, L. Liao, *IEEE Trans. Electron Devices.* **2018**, *65*, 2844.

[50] S. M. Sze, K. K. Ng, *Physics of Semiconductor Devices*, John Wiley & Sons, New York **2006**.

[51] Y. Kim, S. Kim, W. Kim, M. Bae, H. K. Jeong, D. Kong, S. Choi, D. M. Kim, D. H. Kim, *IEEE Trans. Electron Devices.* **2012**, *59*, 2699.

[52] M. J. Kim, H. J. Park, S. Yoo, M. H. Cho, J. K. Jeong, *IEEE Trans. Electron Devices.* **2022**, *69*, 2409.

[53] S. Jeon, S.-E. Ahn, I. Song, C. J. Kim, U-I. Chung, E. Lee, I. Yoo, A. Nathan, S. Lee, J. Robertson, K. Kim, *Nat. Mater.* **2012**, *11*, 301.